# optica

## Acousto-optic modulation of a wavelength-scale waveguide

CHRISTOPHER J. SARABALIS,<sup>1,2</sup> D RAPHAËL VAN LAER,<sup>1</sup> RISHI N. PATEL,<sup>1</sup> D YANNI D. DAHMANI,<sup>1</sup> WENTAO JIANG,<sup>1</sup> FELIX M. MAYOR,<sup>1</sup> AND AMIR H. SAFAVI-NAEINI<sup>1,3</sup>

<sup>1</sup>Department of Applied Physics and Ginzton Laboratory, Stanford University 348 Via Pueblo Mall, Stanford, California 94305, USA <sup>2</sup>e-mail: sicamor@stanford.edu

Received 27 October 2020; revised 17 January 2021; accepted 7 February 2021 (Doc. ID 413401); published 6 April 2021

Since the advent of the laser, acousto-optic modulators have been an important tool for controlling light. Recent advances in on-chip lithium niobate waveguide technology present new opportunities for these devices. We demonstrate a collinear acousto-optic modulator in a suspended film of lithium niobate employing a high-confinement, wavelength-scale waveguide. By strongly confining the optical and mechanical waves, this modulator improves a figure-of-merit that accounts for both acousto-optic and electro-mechanical efficiency by orders of magnitude. Our device demonstration marks a significant technological advance in acousto-optics that promises a novel class of compact and low-power frequency shifters, tunable filters, non-magnetic isolators, and beam deflectors. © 2021 Optical Society of America under the terms of the OSA Open Access Publishing Agreement

https://doi.org/10.1364/OPTICA.413401

### 1. INTRODUCTION

Lithium niobate (LN) has played a central role in the development of acousto-optic (AO) devices. In the decades following the initial demonstration of the AO tunable filter [1], the electrical power consumption of these devices improved from watts to milliwatts through the development of Ti-indiffused and proton-exchanged LN optical and surface acoustic wave (SAW) waveguides and through the development of efficient SAW transducers [2–6]. These waveguides only weakly confine the optical and mechanical fields. The potential for greater confinement and, thereby, larger interaction strengths is an opportunity to again dramatically improve the efficiency and reduce the size of these devices.

In recent years, a new LN waveguide technology has emerged that can vastly improve electro-optic, AO, and nonlinear optical devices. Advances in etch techniques have resulted in low-loss, wavelength-scale optical waveguides [7] in high-quality, single-crystal films of LN [8]. Owing to their high confinement, these waveguides have powered the development of an array of compact, highly efficient nonlinear devices [9–11] and modulators [12–14] for classical and quantum applications. In tandem, LN films have been used to realize low-loss, strongly coupled piezoelectric devices [15–20]. We have recently demonstrated that high-confinement waveguides in this platform can be efficiently piezoelectrically transduced [21] and that these transducers can vastly improve the AO efficiency of nanoscale optomechanical resonators [22]. For many applications, efficient non-resonant AO transduction is desired.

Here, we demonstrate a collinear AO mode converter using high-confinement, wavelength-scale waveguides in suspended,

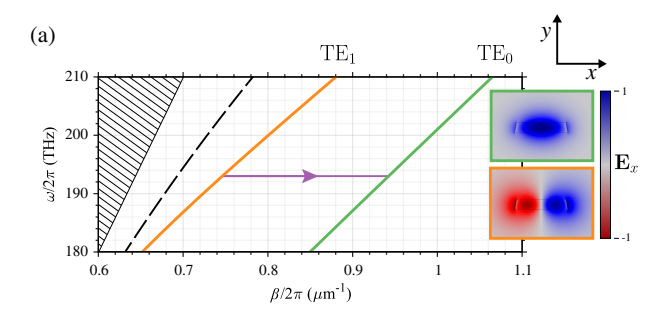
*X*-cut films of LN. After reviewing the physics of these modulators, including methods for calculating the optomechanical coupling coefficient g (Section 2), we discuss how the optical and mechanical modes can be addressed with AO multiplexers (Section 3). We use these multiplexers to realize a frequency-shifting, four-port optical switch near 1550 nm and 440 MHz. We describe the behavior of this device in Section 4. The efficiency of the modulator is characterized in Section 5 and used to back out an interaction strength  $g/\sqrt{\hbar\Omega}$  of 0.38 mm<sup>-1</sup> $\mu$ W<sup>-1/2</sup>, which quantifies the required interaction length and mechanical drive power for full conversion. Owing to this large g, this modulator exhibits a recordlow power consumption for its length, as seen in Table 2. These modulators are inherently nonreciprocal, as demonstrated in Section 5, where we discuss prospects for using them to make nonmagnetic isolators. The results reported here mark a significant advance in guided acousto-optics that could enable a new class of low-power, integrated components.

#### 2. OPTOMECHANICS IN A WAVEGUIDE

The interactions between light and sound have been studied for a long time [29]. Here, we review these interactions for the modes of a waveguide [30–33], specifically in the case where sound scatters light between two optical modes. In the context of Brillouin scattering, this is often called *inter-modal* [34] or *inter-polarization* [35] scattering. In contrast to stimulated Brillouin scattering, here we study how light moves in the presence of a strong mechanical drive, where the light does not affect the dynamics of the sound.

We direct our attention to Fig. 1, which shows the optical and mechanical modes of a LN waveguide. The waveguide supports

<sup>&</sup>lt;sup>3</sup>e-mail: safavi@stanford.edu



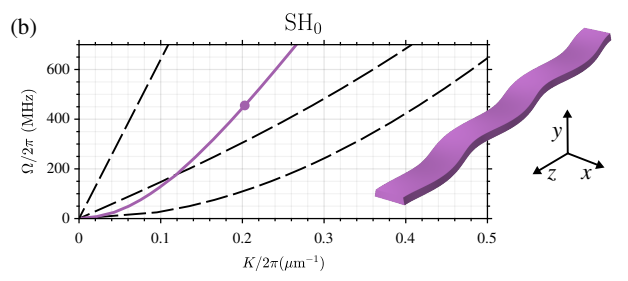


**Fig. 1.** Optical and mechanical band structure of a wavelength-scale waveguide. (a) The LN waveguide investigated supports a TE<sub>0</sub> (green) and TE<sub>1</sub> (orange) mode. The x component of the electric field is plotted showing the TE<sub>1</sub> node on the reflection-symmetry plane. At 193 THz, their wavevectors differ by  $K=2\pi\times0.2~\mu\text{m}^{-1}$  shown with the purple arrow. (b) The fundamental SH<sub>0</sub> mode with this K is plotted alongside the mechanical bands (SH<sub>0</sub> in purple). The mode profiles plotted are used to compute  $g/\sqrt{\hbar\Omega}=1~\text{mm}^{-1}~\mu\text{W}^{-1/2}$ .

a TE<sub>0</sub> mode with the electric field  $a_0\mathbf{e}_0 \exp(i\beta_0z - i\omega_0t) + \text{c.c.}$  and a TE<sub>1</sub> mode with the field  $a_1\mathbf{e}_1 \exp(i\beta_1z - i\omega_1t) + \text{c.c.}$ . It also supports the fundamental horizontal shear (SH<sub>0</sub>) mechanical mode with displacement b  $\mathbf{u} \exp(iKz - i\Omega t) + \text{c.c.}$ , which scatters light between the TE<sub>0</sub> and TE<sub>1</sub> modes. The mode profiles  $\mathbf{e}_i$  and  $\mathbf{u}$  are complex vector fields on the xy plane. They are normalized such that  $|a_i|^2$  and  $|b|^2$  are the photon and phonon number flux with units of hertz (Hz).

When the scattering process is phase-matched, e.g.,  $\omega_1 + \Omega = \omega_0$  and  $\beta_1 + K = \beta_0$ , as shown in Fig. 1(a), the coefficients  $\mathbf{a}(t,z) = (a_0(t,z), a_1(t,z))^{\mathrm{T}}$  obey

$$\left(\mathbf{v}^{-1}\partial_t + \partial_z\right)\mathbf{a} = -ig\,b\sigma_x\mathbf{a},\tag{1}$$

as shown in Supplement 1, Section 1. Here,  $\mathbf{v}$  is a diagonal matrix containing the optical group velocities, g is the optomechanical coupling coefficient, and  $\sigma_x$  is the Pauli-X matrix. In Eq. (1), we assume that b is real.

In the absence of coupling  $g \to 0$ , light in the two modes propagate independently according to a telegrapher equation. When we turn on the coupling, light oscillates between the modes (see Fig. 1 and Table 1):

$$\mathbf{a} = \exp(-ig\,bz\sigma_x)\,\mathbf{a}_0 = \begin{pmatrix} \cos\zeta & -i\sin\zeta \\ -i\sin\zeta & \cos\zeta \end{pmatrix}\mathbf{a}_0, \qquad (2)$$

where  $\zeta \equiv g\,bz$ , and  $\mathbf{a}_0$  is the vector of the initial coefficients at z=0. These steady-state solutions assume that b is uniform along the waveguide, but we consider a more general case with loss and detuning in Supplement 1, Section 2. Like a bulk AO modulator (AOM), a waveguide-based modulator is a frequency-shifting switch. When  $\zeta = \pi/2$ , light initially in mode 0 is converted to mode 1 before being converted back to mode 0 at  $\zeta = \pi$ .

Table 1. Simulated Effective and Group Indices for the Optics at 1550 nm and the Wavelength and Group Velocity for the Mechanics that Phase-Matches These Optical Modes

Mode	$n_{ m eff}$	$n_{ m g}$	
$\overline{\text{TE}_0}$	1.464	2.147	
$TE_0$ $TE_1$	1.159	2.288	
Mode	$2\pi/\mathrm{K}$	v	
SH <sub>0</sub>	5.081 μm	3623 m/s	

Confining light and sound to a wavelength-scale waveguide enhances the interaction strength g, enabling smaller, more efficient devices. This can be seen in the expression for the coupling coefficient from mode 1 into mode 0:

$$g_{01} = -\frac{\omega_0}{2} \frac{\int dA \, \mathbf{e}_0^* \delta_{\mathbf{u}} \varepsilon \cdot \mathbf{u} \mathbf{e}_1}{\mathcal{P}_0 \sqrt{\mathcal{P}_{\mathbf{m}} / \hbar \Omega}}.$$
 (3)

Here,  $\mathcal{P}_i$  is the optical power in mode i when  $|a_i|^2 = 1$ ,  $\mathcal{P}_{\rm m}$  is the mechanical power when  $|b|^2 = 1$ , and  $\delta_{\bf u} \varepsilon \cdot {\bf u}$  encodes the permittivity shift from the deformation  ${\bf u}$ , as described in Supplement 1, Section 1. First, we note how this expression relates to g in Eq. (1). By choosing a flux-normalized basis where  $\mathcal{P}_i = \hbar \omega_i$ , the coupling takes a Hermitian form  $g_{ij} = g_{ji}^*$ . This can be made real and symmetric by the choice of the phase of the mode profiles, giving us the g used in Eq. (1) [36].

Next, we consider how g scales with the area of a waveguide. In the limit of high confinement, small changes to a waveguide's geometry change its dispersion and the shape of its modes. For fixed  $\omega$ , g has a complicated dependence on waveguide geometry. When the waves are weakly confined, the numerator in Eq. (3),  $\mathcal{P}_0$ , and  $\mathcal{P}_m$  are approximately proportional to the area of the waveguide A. In this regime, the factors of A from the numerator and  $P_0$  cancel, leaving only  $A^{-1/2}$  from  $P_m$ . Intuitively, it takes more power  $P_m$  to deform a larger waveguide by  $\mathbf{u}$ , which comes at the expense of g and, ultimately, a device's efficiency. Other three-wave processes like electro-optic and  $\chi^{(2)}$  interactions scale similarly. This motivates the pursuit of high-confinement waveguides for nonlinear and parametric processes like acousto-optics, underlying recent activity in thin-film LN.

We can use Eq. (3) to calculate the coupling for the rectangular waveguide studied here. Our waveguide is patterned into X-cut LN with the extraordinary axis perpendicular to the waveguide (parallel to the x axis in the figures). This orientation is chosen to efficiently excite the SH mode. The waveguide is suspended by etching the silicon substrate. It is  $1.25~\mu m$  wide and 250~nm thick. We define the waveguide in a hydrogen silsesquioxane mask and transfer it to the LN film with an argon ion mill. This produces a  $10^\circ$  sidewall angle that is included in the simulations. The mode profiles plotted in Fig. 1 are used to compute the coupling coefficient

$$\frac{g}{\sqrt{\hbar\Omega}} = 1.0 \frac{1}{\text{mm}\sqrt{\mu W}}.$$
 (4)

With this coupling, approximately  $40~\mu W$  in the  $SH_0$  mode would completely transfer light from the  $TE_0$  to the  $TE_1$  mode (or vice versa) over just  $250~\mu m$  in the waveguide.

Table 2.	Low- and High-Confinement Collinear AOMs <sup>a</sup>
iable 2.	Low- and riight-comment comment Acids

Work	Year	λ (nm)	$\Omega/2\pi$ (MHz)	L (mm)	$P_{\pi/2}$ (mW)	γ (dB/mm)	$ t_{b\mu} ^2$ (dB)	$g/\sqrt{\hbar\Omega}$ (mm <sup>-1</sup> W <sup>-</sup>	$(L/\lambda)^2 P_{\pi/2}$ $^{1/2})$ (MW)	$\eta_{\mathrm{max}}$ (%)
Harris [1]	1970	632.8	54	35	$3.64 \times 10^{3}$	_	-7.5	0.057	$1.1 \times 10^{4}$	95
Ohmachi [2]	1977	1150	245.5	4.5	550	_	-20	4.7	8.42	70
Binh [3]	1980	632.8	550	9	225	_	-25	6.54	45.5	99
Heffner [23]	1988	1523	175	25	500	_	-7.0	0.20	135	97
Hinkov [24]	1988	633	191.62	17	400	-0.1	-25	2.6	289	90
Frangen [25]	1989	1520	178	9	90	-0.05	-10	1.9	3.16	99
Hinkov [26]	1991	800	355.5	20	19.8	-0.04	-3	0.825	12.4	93
Hinkov [5]	1994	800	365	25	0.5	$-0.04^{b}$	$-3^{b}$	4.2	0.488	100
Duchet [6]	1995	1556	170	30	6	_	-3	0.96	2.23	100
Liu [27]	2019	1510	16,400	0.5	$4.2 \times 10^{5}$	_	-15	0.041	46.4	$2.5 \times 10^{-4}$
Kittlaus [28]	2020	1600	3110	0.240	$4.69 \times 10^{3}$		-12	5.7	0.105	1
Kittlaus [28] <sup>c</sup>	2020	1525.4	3110	0.960	$1.48 \times 10^{3}$	_	-12	4.5	0.587	13.5
This work	2020	1550	440	0.25	60	-11.7	-21.9	377	$1.6 \times 10^{-3}$	18

"We extend the table compiled by Smith et al. [4] to include estimates for  $t_{b\mu}$  and g and recent work on high-confinement waveguide devices.  $\eta_{max}$  is the maximum conversion efficiency demonstrated. The values for g are inferred from  $P_{\pi/2}$ . We account for mechanical propagation loss where reported. High-confinement modulators dramatically improve the figure-of-merit  $(L/\lambda)^2 P_{\pi/2}$ .

### 3. ADDRESSING THE OPTICAL AND ACOUSTIC MODES OF A WAVEGUIDE

In order to use these interactions to build devices, we need to efficiently address each of the optical and mechanical modes in our waveguide. To this end, we engineer the AO multiplexer [37] shown in Fig. 2. This device separates the TE<sub>0</sub> optical, TE<sub>1</sub> optical, and SH<sub>0</sub> acoustic waves into three ports and couples them off-chip.

Light and sound behave very differently at the boundary of a waveguide. Mechanical energy is only transferred between two bodies if they touch. On the other hand, light can tunnel across a

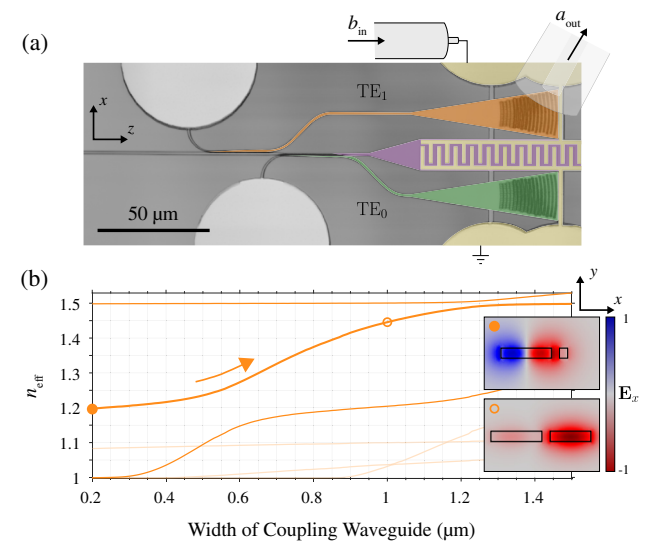


**Fig. 2.** Addressing the modes with an AO multiplexer. (a) Light can be injected into the  $TE_0$  and  $TE_1$  modes of the waveguide through the green and orange optical ports, respectively. The  $SH_0$  mechanical mode of the waveguide is excited by the purple piezoelectric transducer. (b) The optical mode injectors ( $TE_1$  shown) adiabatically transfer the mode from the waveguide into the  $TE_0$  mode of the coupler by tapering the width of the coupling waveguide.

gap between adjacent dielectrics. We can use this fundamental difference when designing a multiplexer to evanescently transfer light between adjacent waveguides without disturbing the mechanics.

The optical mode multiplexer comprises two adiabatic tapers. The first on the left of Fig. 2(a) and closer to the AO waveguide couples to the TE<sub>1</sub> mode and the second to the TE<sub>0</sub> mode. This design is similar to the cascaded mode injector developed by Chang et al. to use multi-moded waveguides for compact, low-drive power phase shifters [38]. In our coupler, the 1.25-µm-wide AO waveguide supports a TE<sub>0</sub> and TE<sub>1</sub> mode. The TE<sub>1</sub> mode is close to cutoff and has long evanescent tails. Starting from the left, a 200-nm-wide coupling waveguide is brought in to a distance 200 nm from the AO waveguide. As the width is increased, the  $TE_0$ mode of the coupling waveguide hybridizes with the TE<sub>1</sub> mode of the AO waveguide, leading to the anti-crossing in Fig. 2(b) near 600 nm. The coupling waveguide is tapered up to 1 µm in width over 25 µm, and the AO waveguide's TE<sub>1</sub> mode is adiabatically transferred into the coupler's TE<sub>0</sub>. The coupler waveguide is then bent away from the AO waveguide and sent to the top grating coupler in Fig. 2(a). After coupling out TE<sub>1</sub>, the AO waveguide is narrowed to 575 nm such that TE<sub>0</sub> exhibits long evanescent tails, and the process is repeated for the TE<sub>0</sub> mode, this time tapering the coupler from 400 nm to 1 µm.

We measure the optical transmission through the device in Fig. 3. Our best device exhibited -5 dB insertion loss, excluding the grating couplers and -10 dB crosstalk, i.e., unintended scatter from the  $TE_0$  (or  $TE_1$ ) input port to the  $TE_1$  ( $TE_0$ ) output port. This crosstalk causes the carrier to leak into ports where, in an ideal device, only an up- or down-shifted sideband would be transmitted. It can be further reduced by optimizing the device or by actively compensating for crosstalk with an electrically tunable feed network [39].

The silicon substrate is etched away, releasing the LN waveguides such that they support optical and mechanical waves. Releasing the device causes the AO and coupling waveguides to deviate from the plane of the chip by different amounts, separating and decoupling the waveguides. To prevent this, we add 150-nm-wide tethers at the ends of each coupling waveguide. These tethers

Value copied from Ref. [26].

The two rows are for the straight (top) and serpentine (bottom) modulators reported. These devices are side-coupled, not collinear.

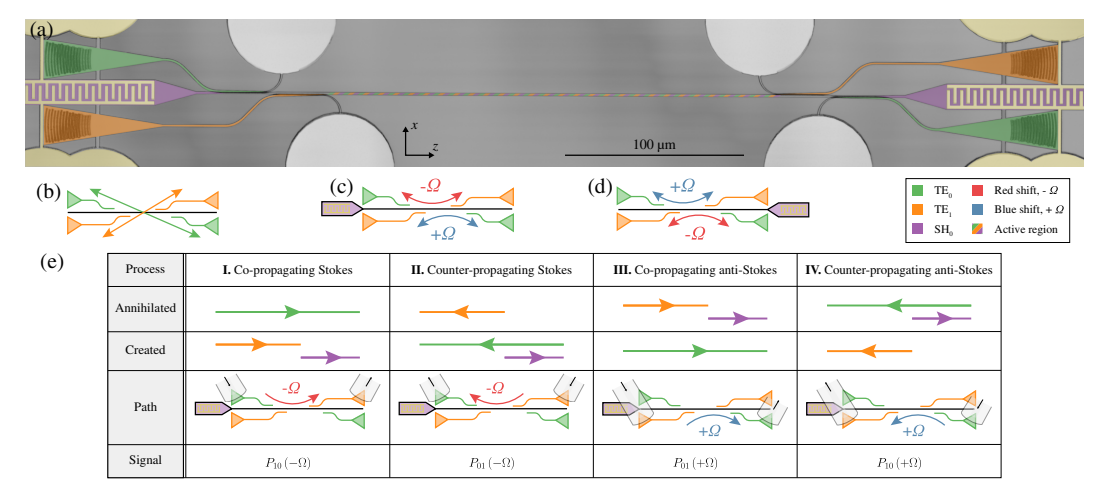


**Fig. 3.** Integrated AOM. (a) The full modulator comprises two multiplexers described in Section 3 and a waveguide where the interactions happen, labeled "active region." It constitutes a four-optical-port, frequency-shifting switch. (b) When no phonons are in the waveguide, light propagates along cross-shaped paths. (c) When the left transducer is driven, photons that emit/absorb a phonon travel along the top/bottom bar-shaped path. (d) If we change the direction of the phonons, the emission/absorption paths are switched. (e) We tabulate the four AO processes that govern the device when driven from the left (c), including the resulting heterodyne signal, as described in Section 5.

can scatter mechanical waves in the AO waveguide, counter to the design strategy.

Mechanical waves in the waveguide are coupled out with a piezoelectric transducer after the optical couplers. We adapt the transducer design presented in Ref. [21] for the frequency range of interest. The rescaled design excites the fundamental SH mode with  $K = 2\pi/5.08 \ \mu m^{-1}$  that can phasematch the TE<sub>0</sub> and TE<sub>1</sub> optical modes at 1550 nm. The interdigital transducer (IDT) is patterned by lift-off into 200 nm of evaporated aluminum. It has 35 finger pairs with a pitch of 7  $\mu m$  and width of 13.2  $\mu m$ .

We measure the *S* matrix of this two-port microwave system on a calibrated probe station and extract the mechanical propagation loss  $\gamma = 11.7$  dB/mm and the efficiency of the transducer  $|t_{b\mu}|^2 = -21.9$  dB.  $t_{b\mu}$  is the amplitude transmission coefficient from a 50  $\Omega$  transmission line into the SH<sub>0</sub> mode of the AO waveguide [21]. The peak conductance of these transducers is 2.3 mS, and, as a result, 4.3 dB of the insertion loss comes from impedance mismatch. The rest is likely from material damping in the transducer [21].

A more detailed characterization of the multiplexer, including its frequency response, is presented in Supplement 1, Section 3.

### 4. WAVEGUIDE AO MODULATOR

The multiplexers described in the previous section give us access to the optical and mechanical modes of the modulator in Fig. 3. All four phase-matched processes—co- and counter-propagating, Stokes and anti-Stokes—are at play in this four-port, frequency-shifting switch.

First, we consider what happens without the mechanical drives. We send light at  $\omega$  into the bottom-left grating (orange), which gets injected into the  $TE_1$  mode of the waveguide. With no phonons in the waveguide, the light passes through the device and gets removed by the  $TE_1$  injector, leaving the chip from the top-right grating (orange). The optical paths through an undriven device are shown in Fig. 3(b).

Now, consider the co-propagating anti-Stokes process [Fig. 3 (e. III)]. Again sending light into the bottom-left, we drive the left

transducer with an RF tone at  $\Omega$ . This sends phonons down the waveguide to the right. Photons in the  $TE_1$  mode of the waveguide absorb co-propagating phonons and scatter into the  $TE_0$  mode. After absorption, their frequency increases to  $\omega + \Omega$ , and their wavevector increases from  $\beta_1(\omega)$  to  $\beta_0(\omega + \Omega) = \beta_1(\omega) + K$  (also shown in Fig. 1). The  $TE_0$  injector removes these up-shifted photons from the waveguide, and they are scattered off-chip by the grating in the bottom-right (green).

If we instead send light into  $TE_0$  from the top-left (green), the co-propagating phonons stimulate emission—instead of absorption—and the incident light scatters into the  $TE_1$  mode at  $\omega - \Omega$ . The down-shifted light leaves the chip through the top-right grating (orange). This is the co-propagating Stokes process diagrammed in Fig. 3(e. I).

In addition to the two co-propagating processes described above, there are counter-propagating processes that we probe by sending the optical field from right to left [Fig. 3(e. II, IV)]. The four processes are summarized in Fig. 3(c). The co-propagating and counter-propagating Stokes processes—e. I and e. II, respectively—form the top red-shifted path. The co- and counter-propagating anti-Stokes processes—III and IV—form the bottom blue-shifted path. When  $L_{\rm eff}\gg\Omega^{-1}(v_1^{-1}+v_0^{-1})^{-1}$ , the co- and counter-propagating processes are not simultaneously phase-matched.

Driving the mechanics from the right, i.e., flipping the direction of the phonon, also switches absorption and emission. This gives us Fig. 3(d), which, because of the symmetry of our device, is equivalent to Fig. 3(c) under a 180° rotation.

We can think of the device as a frequency-shifting optical switch. No matter which direction the phonons are coming from, the mechanical drive switches the device from the "cross" state [Fig. 3(b)] to the "bar" state [Figs. 3(c) and 3(d)]. The direction of the mechanical wave determines which path red shifts and which path blue shifts the light.

### 5. CHARACTERIZING THE MODULATION

In addition to the mechanical efficiency and attenuation reported in Section 3, g is a key figure that determines the modulator's efficiency. We determine g by measuring the scattered power and pump depletion using the heterodyne setup in Fig. 4(a). Light in the telecom C band is generated with a Santec TSL-550 laser. It is split with half of the light sent to the device and the other half up-shifted by  $\Delta \equiv 2\pi \times 200$  MHz using an AOM. The paths are recombined with a 99:1 splitter and sent to an Optilab PD-40-M detector. The photocurrent spectrum  $S_{II}[\omega]$  is measured with a Rhode & Schwartz FSW spectrum analyzer.

A photocurrent spectrum of the co-propagating anti-Stokes process [Fig. 3(e. III)] for a device with  $L=250~\mu m$  is shown in Fig. 4(b) for a drive frequency of  $\Omega=2\pi\times440~MHz$ . There are three important tones in the spectrum: one at  $\Delta$  and the other two at  $\Omega\pm\Delta$ . If the light travels through the device without being scattered by the acoustic wave, its frequency stays the same, leading to the RF tone at 200 MHz. If the light absorbs/emits a phonon from the acoustic field, its frequency is shifted by  $\pm440~MHz$ , generating the tone at 240/640 MHz. We denote the power in these tones  $P_{ij}(\omega')$ , where ij specifies the optical path  $TE_i \to TE_i$ ,

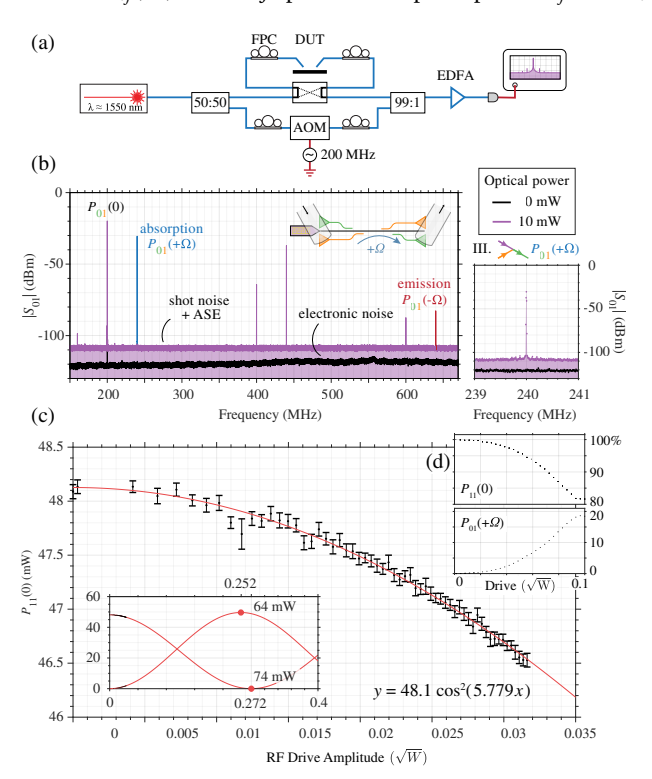


**Fig. 4.** Heterodyne measurements. (a) Schematic of the optical heterodyne receiver. FPC, fiber polarization controller; DUT, device under test; EDFA, erbium-doped fiber amplifier. (b). An example photocurrent spectrum of the co-propagating anti-Stokes process for a 440 MHz drive. The three tones of interest are the unscattered pump  $P_{01}(0)$  at 200 MHz, the absorption signal  $P_{01}(+\Omega)$  at 240 MHz, and the emission signal  $P_{01}(-\Omega)$  at 640 MHz, which is suppressed by over 50 dB. ASE, amplified spontaneous emission. (c) Fitting a sinusoid to the pump depletion  $P_{11}(0)$ , we extrapolate the full-conversion drive power  $P_{\pi/2}$  (inset bottom-left), which is used to determine g. The absorption signal  $P_{01}(+\Omega)$  gives us a similar result. (d) At higher drive powers, the signal deviates from a sinusoid (Supplement 1, Section 4). We observe up to 18% conversion corresponding to 30 μW in the SH<sub>0</sub> mode of the waveguide. The signal has been normalized by the undepleted pump [ $P_{11}(0)$  with the drive off].

and  $\omega + \omega'$  is the frequency of the light generating the tone. The power,

$$P_{01}(+\Omega) = Z_0 \int_{-B/2}^{B/2} d\omega \, S_{II} \left[\Omega - \Delta + \omega\right] \tag{5}$$

for our example process, is proportional to the optical power emitted from the device. Here,  $Z_0$  is 50 Ohms, and B is the integration bandwidth. Each process in Fig. 3(e) is labeled with the resulting  $P_{ij}(\omega')$ .

By fitting the scattered power  $P_{10}(+\Omega)$  and pump depletion  $P_{11}(0)$ , we determine g in a way that is insensitive to the calibration of the loss in the optical signal chain (Supplement 1, Section 5). For a phase-matched process, these fits [Fig. 4(c)] give us  $g t_{\rm b\mu} L_{\rm eff}/\sqrt{\hbar\Omega}$ , where

$$L_{\text{eff}} = 2\gamma^{-1} \left[ 1 - \exp\left(-\gamma L/2\right) \right],$$
 (6)

as described in Supplement 1, Section 2. In Fig. 4(c), we extrapolate  $P_{\pi/2}$ , the power it takes to fully swap  $TE_1 \leftrightarrow TE_0$ , which is related to g as

$$g h_{\rm b\mu} L_{\rm eff} \sqrt{\frac{P_{\pi/2}}{\hbar \Omega}} = \frac{\pi}{2}.$$
 (7)

After removing the cable loss (0.6 dB), we find

$$\frac{g}{\sqrt{\hbar\Omega}} = 0.38 \frac{1}{\text{mm}\sqrt{\mu W}},\tag{8}$$

roughly a third of the simulated value. This discrepancy is similar to what we have observed for waveguides in LN films on sapphire [14] and resonant optomechanical systems in suspended LN films [40].

To better understand the different device architectures, we extend the table presented by Smith *et al.* [4] to include  $t_{b\mu}$ , g, and recent work with high-confinement waveguides (Table 2). If the conversion efficiency  $P_{\pi/2}$  is not directly measured, we extrapolate  $P_{\pi/2}$  from low-power measurements of the efficiency. The transducer's transmission  $t_{b\mu}$  is not typically reported. Here, we de-embed  $t_{b\mu}$  from the two-port S parameter (Supplement 1, Section 3.3). Without careful analysis,  $t_{b\mu}$  is prone to overestimate. For example, Rayleigh and Bleustein-Gulyaev waves are nearly degenerate for X-cut LN devices [5,23,25,26] and, if not properly handled, degrade  $t_{b\mu}$  without reducing  $|S_{21}|$  [6]. Where we are unable to infer  $t_{b\mu}$ , we assume  $|t_{b\mu}|^2 + |S_{11}|^2 = 1$ , which strictly over-estimates  $|t_{b\mu}|$ . The optomechanical coupling coefficient is inferred from  $t_{\rm b\mu}$  and  $P_{\pi/2}$ , taking into account mechanical loss  $\gamma$  where reported. The figure-of-merit  $(L/\lambda)^2 P_{\pi/2}$  is adapted from Smith *et al.* [4]. It is proportional to  $|gt_{b\mu}|^{-2}$ . A low-power, compact modulator requires a low figure-of-merit, i.e., both an efficient transducer and strong photon-phonon interactions.

AOMs are inherently nonreciprocal and can be used to make isolators and circulators to stabilize lasers [41] and to help manage reflections in large photonic circuits. Nonreciprocal components usually employ the magneto-optical effect, motivating the pursuit of thin-film yttrium iron garnet (YIG) functional layers in silicon photonics [42,43]. Alternatively, parametric drives like acousto-optics give us a non-magnetic way to build nonreciprocal components [28,41,44–51].

In these devices, nonreciprocity takes a slightly different form than in a standard isolator. Consider the bottom path in Fig. 3(c). Light traveling between the  $TE_1$  and  $TE_0$  ports absorbs a phonon independent of the direction the light travels. This can be seen

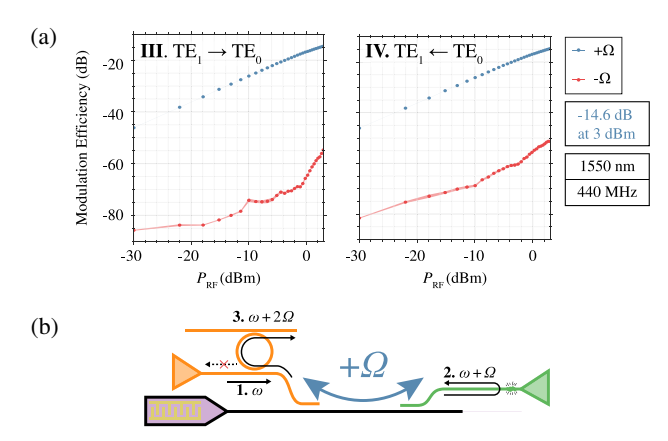


**Fig. 5.** Nonreciprocal, direction-independent frequency shift. (a) Light traveling along the bottom path of Fig. 3(c) incurs  $a + \Omega$  blue shift independent of the direction it travels. This is a signature of nonreciprocity. Here, *modulation efficiency* is the scattered power over the undepleted pump, e.g.,  $P_{01}(+\Omega)$  over  $P_{11}(0)$  for III. (b) The resulting round-trip frequency-shift can be used to build a frequency-shifting isolator. A ring filter can be added before the AOM to drop reflections.

directly in the path-independent blue shift measured in Fig. 5(a). If light takes a round-trip through the device, it absorbs two phonons and returns to a different state.

This round-trip frequency shift is nonreciprocal. It can be used to build the frequency-shifting isolator in Fig. 5(b) [44]. Light back-scattered from, e.g., an imperfect component, is shifted by  $+2\Omega$  and, as a result, can be dropped by a filter to isolate the input port from reflections. When  $L_{\rm eff} \gg v_1/2\Omega$ , the backwards process is not phase-matched, and the reflections are dropped even without a filter [28]. Finally, this device can be cascaded with another AOM to make a fixed-frequency isolator [45].

### 6. OUTLOOK

Building off of our recent work on waveguide transduction [21], we demonstrate a compact AOM in a suspended film of X-cut LN. The modulator comprises a frequency-shifting, four-port optical switch at 440 MHz and 1550 nm. By employing high-confinement optical and mechanical modes with strong photon–phonon interactions  $(g/\sqrt{\hbar\Omega}=0.38~{\rm mm}^{-1}\mu{\rm W}^{-1/2})$ , it exhibits a record-setting figure-of-merit. This device is optically broadband with a 3 dB bandwidth of 40 nm (Supplement 1, Section 2.2) and, as demonstrated, is inherently nonreciprocal. We discuss how it can be integrated with an optical filter to implement a fixed-frequency, non-magnetic isolator.

High-confinement waveguides mark a significant advance in the figure-of-merit of collinear AOMs. The device reported here offers a two order-of-magnitude increase in g and a  $1,000\times$  improvement in the figure-of-merit over Ti-indiffused and proton-exchanged waveguides. While high-confinement AOMs have yet to achieve full conversion or a record  $P_{\pi/2}$ , both are within reach. There is room to improve the transducer. Piezoelectric waveguide transducers similar to the ones used here but centered at 2 GHz [21] are nearly 10 dB more efficient. Recovering that 10 dB—for example, through design improvements—would yield full conversion. With a modest length increase (e.g., L=1 mm),  $P_{\pi/2}$  would drop below a milliwatt.

Reducing the loss in these high-confinement mechanical waveguides could dramatically lower the necessary drive power.

The mechanical loss measured here,  $\gamma=11.7\,\mathrm{dB/mm}$ , limits  $L_{\mathrm{eff}}$  to 742 µm. At similar frequencies, low-confinement devices exhibit a  $\gamma$  as small as 0.04 dB/mm [26] and, therefore,  $L_{\mathrm{eff}}$  as long as 22 cm. Recently, high-confinement mechanical waveguides in GaN-on-sapphire have been demonstrated with  $\gamma=0.05\,\mathrm{dB/mm}$  at 192 MHz [52]. Increasing  $L_{\mathrm{eff}}$  from 250 µm to 1 cm/10 cm decreases  $P_{\pi/2}$  by  $-32\,\mathrm{dB/}-52\,\mathrm{dB}$  with another  $-22\,\mathrm{dB}$  available from improvements to  $t_{\mathrm{b}\mu}$ . Without increasing g,  $P_{\pi/2}$  could be as low as a nanowatt.

A long effective length not only improves efficiency, it is necessary for narrow bandwidth optical filtering. A typical commercial AO tunable filter offers nanometer-scale bandwidth. The 3 cm length of the AO tunable filter in Ref. [26] enabled a bandwidth of 0.32 nm. For high-confinement waveguides to realize compelling filter functions, we need either better mechanical waveguides or to distribute the mechanical transduction along the waveguide (*e.g.*, multiple side-coupled transducers in the architecture in Ref. [28]).

Lastly, switching to an unsuspended platform presents opportunities to integrate AO components into larger, more complex circuits and systems, which draw from the growing toolbox of piezoelectric, electro-optic, nonlinear, and even quantum components in thin-film LN. Such a switch could also improve the power handling and robustness of the devices. One candidate is LN-on-sapphire, which exhibits good AO and piezoelectric properties [14], and in which efficient waveguide transducers have been recently demonstrated [20].

The AOM presented here marks an advance of a rapidly developing waveguide technology and material platform. AO devices like this could soon play a role as compact, low-power frequency-shifters, non-magnetic isolators, tunable filters, and beam deflectors in complex circuits and systems.

**Funding.** National Science Foundation (ECCS-1542152, ECCS-1808100, PHY-1820938); U.S. Air Force (FA955550-17-1-0002); Nippon Telegraph and Telephone; Defense Advanced Research Projects Agency (Young Faculty Award); David and Lucile Packard Foundation.

**Acknowledgment.** The authors thank NTT Research Inc. for their financial and technical support. Part of this work was performed at the Stanford Nano Shared Facilities (SNSF), supported by the National Science Foundation, and the Stanford Nanofabrication Facility (SNF).

C.J.S. led the project and wrote the manuscript with help from R.V.L. and A.H.S.-N. R.V.L. and R.N.P. contributed to the measurements, Y.D.D. to the development of the piezoelectric transducers, and W.J. and F.M.M. to the development of the fabrication process. A.H.S.-N. supervised the project.

**Disclosures.** The authors declare no conflicts of interest.

**Supplemental document.** See Supplement 1 for supporting content.

### **REFERENCES AND NOTE**

- S. Harris, S. Nieh, and R. Feigelson, "CaMoO<sub>4</sub> electronically tunable optical filter," Appl. Phys. Lett. 17, 223–225 (1970).
- Y. Ohmachi and J. Noda, "LiNbO<sub>3</sub> TE-TM mode converter using collinear acoustooptic interaction," IEEE J. Quantum Electron. 13, 43–46 (1977).
- L. Binh, J. Livingstone, and D. Steven, "Tunable acousto-optic TE-TM mode converter on a diffused optical waveguide," Opt. Lett. 5, 83–84 (1980).
- D. A. Smith, J. E. Baran, J. J. Johnson, and K.-W. Cheung, "Integrated-optic acoustically-tunable filters for WDM networks," IEEE J. Sel. Areas Commun. 8, 1151–1159 (1990).
- I. Hinkov, V. Hinkov, and E. Wagner, "Low power integrated acoustooptical tunable filters in first telecommunication window," Electron. Lett. 30, 1884–1885 (1994).
- C. Duchet, C. Brot, and M. Di Maggio, "Interdigital transducer for acousto-optic tunable filter on LiNbO<sub>3</sub>," Electron. Lett. 31, 1235–1237 (1995).

 C. Wang, M. J. Burek, Z. Lin, H. A. Atikian, V. Venkataraman, I.-C. Huang, P. Stark, and M. Lončar, "Integrated high quality factor lithium niobate microdisk resonators," Opt. Express 22, 30924–30933 (2014).

- M. Levy, R. Osgood, Jr., R. Liu, L. Cross, G. Cargill, III, A. Kumar, and H. Bakhru, "Fabrication of single-crystal lithium niobate films by crystal ion slicing," Appl. Phys. Lett. 73, 2293–2295 (1998).
- L. Chang, Y. Li, N. Volet, L. Wang, J. Peters, and J. E. Bowers, "Thin film wavelength converters for photonic integrated circuits," Optica 3, 531– 535 (2016).
- A. Rao, M. Malinowski, A. Honardoost, J. R. Talukder, P. Rabiei, P. Delfyett, and S. Fathpour, "Second-harmonic generation in periodically-poled thin film lithium niobate wafer-bonded on silicon," Opt. Express 24, 29941–29947 (2016).
- M. Yu, C. Wang, M. Zhang, and M. Lončar, "Chip-based lithium-niobate frequency combs," IEEE Photon. Technol. Lett. 31, 1894–1897 (2019).
- C. Wang, M. Zhang, X. Chen, M. Bertrand, A. Shams-Ansari, S. Chandrasekhar, P. Winzer, and M. Lončar, "Integrated lithium niobate electro-optic modulators operating at CMOS-compatible voltages," Nature 562, 101–104 (2018).
- T. P. McKenna, J. D. Witmer, R. N. Patel, W. Jiang, R. Van Laer, P. Arrangoiz-Arriola, E. A. Wollack, J. F. Herrmann, and A. H. Safavi-Naeini, "Cryogenic microwave-to-optical conversion using a triply-resonant lithium niobate on sapphire transducer," Optica 7, 1737–1745 (2020).
- C. J. Sarabalis, T. P. McKenna, R. N. Patel, R. Van Laer, and A. H. Safavi-Naeini, "Acousto-optic modulation in lithium niobate on sapphire," APL Photon. 5, 086104 (2020).
- R. H. Olsson, III, K. Hattar, S. J. Homeijer, M. Wiwi, M. Eichenfield, D. W. Branch, M. S. Baker, J. Nguyen, B. Clark, T. Bauer, and T. A. Friedmann, "A high electromechanical coupling coefficient SH0 lamb wave lithium niobate micromechanical resonator and a method for fabrication," Sens. Actuators A 209, 183–190 (2014).
- G. Vidal-Álvarez, A. Kochhar, and G. Piazza, "Delay lines based on a suspended thin film of X-cut lithium niobate," in *IEEE International Ultrasonics Symposium (IUS)* (IEEE, 2017), pp. 1–4.
- F. V. Pop, A. S. Kochhar, G. Vidal-Alvarez, and G. Piazza, "Laterally vibrating lithium niobate MEMS resonators with 30% electromechanical coupling coefficient," in *IEEE 30th International Conference on Micro Electro Mechanical Systems (MEMS)* (IEEE, 2017), pp. 966–969.
- T. Manzaneque, R. Lu, Y. Yang, and S. Gong, "Low-loss and wideband acoustic delay lines," IEEE Trans. Microw. Theory Tech. 67, 1379–1391 (2019).
- C. J. Sarabalis, Y. D. Dahmani, A. Y. Cleland, and A. H. Safavi-Naeini, "S-band delay lines in suspended lithium niobate," J. Appl. Phys. 127, 054501 (2020).
- F. M. Mayor, W. Jiang, C. J. Sarabalis, T. P. McKenna, J. D. Witmer, and A. H. Safavi-Naeini, "Gigahertz phononic integrated circuits on thin-film lithium niobate on sapphire," Phys. Rev. Appl. 15, 014039 (2021).
- Y. D. Dahmani, C. J. Sarabalis, W. Jiang, F. M. Mayor, and A. H. Safavi-Naeini, "Piezoelectric transduction of a wavelength-scale mechanical wavequide." Phys. Rev. Appl. 13, 024069 (2020).
- W. Jiang, C. J. Sarabalis, Y. D. Dahmani, R. N. Patel, F. M. Mayor, T. P. McKenna, R. Van Laer, and A. H. Safavi-Naeini, "Efficient bidirectional piezo-optomechanical transduction between microwave and optical frequency," Nat. Commun. 11, 1166 (2020).
- B. Heffner, D. Smith, J. Baran, A. Yi-Yan, and K. Cheung, "Integrated-optic acoustically tunable infra-red optical filter," Electron. Lett. 24, 1562–1563 (1988).
- V. Hinkov, R. Opitz, and W. Sohler, "Collinear acoustical TM-TE mode conversion in proton exchanged Ti:LiNbO<sub>3</sub> waveguide structures," J. Lightwave Technol. 6, 903–908 (1988).
- J. Frangen, H. Herrmann, R. Ricken, H. Seibert, W. Sohler, and E. Strake, "Integrated optical, acoustically tunable wavelength filter," Electron. Lett. 25, 1583–1584 (1989).
- I. Hinkov and V. Hinkov, "Integrated acousto-optic collinear TE-TM mode convertors for 0.8 μm optical wavelength range," Electron. Lett. 27, 1211–1213 (1991).

- Q. Liu, H. Li, and M. Li, "Electromechanical Brillouin scattering in integrated optomechanical waveguides," Optica 6, 778–785 (2019).
- E. A. Kittlaus, W. M. Jones, P. T. Rakich, N. T. Otterstrom, R. E. Muller, and M. Rais-Zadeh, "Electrically-driven acousto-optics and broadband non-reciprocity in silicon photonics," Nat. Photonics 15, 43–52 (2020).
- 29. L. Brillouin, "Diffusion de la lumière et des rayons X par un corps transparent homogène," Ann. Phys. 9, 88–122 (1922).
- C. Wolff, M. J. Steel, B. J. Eggleton, and C. G. Poulton, "Stimulated Brillouin scattering in integrated photonic waveguides: forces, scattering mechanisms, and coupled-mode analysis," Phys. Rev. A 92, 013836 (2015).
- J. Sipe and M. Steel, "A Hamiltonian treatment of stimulated Brillouin scattering in nanoscale integrated waveguides," New J. Phys. 18, 045004 (2016).
- 32. R. Van Laer, R. Baets, and D. Van Thourhout, "Unifying Brillouin scattering and cavity optomechanics," Phys. Rev. A 93, 053828 (2016).
- B. J. Eggleton, C. G. Poulton, P. T. Rakich, M. J. Steel, and G. Bahl, "Brillouin integrated photonics," Nat. Photonics 13, 664–677 (2019).
- 34. E. A. Kittlaus, N. T. Otterstrom, and P. T. Rakich, "On-chip inter-modal Brillouin scattering," Nat. Commun. 8, 15819 (2017).
- M. S. Kang, A. Butsch, and P. St.J. Russell, "Reconfigurable light-driven opto-acoustic isolators in photonic crystal fibre," Nat. Photonics 5, 549– 553 (2011).
- 36. If we normalize such that  $|b|^2$  is power instead of flux, the factors of  $\sqrt{\hbar\Omega}$  disappear from g and throughout the text.
- 37. N. Dostart and M. Popović, "Multiplexing guided optical and acoustic waves for efficient acousto-optic devices," arXiv:2007.11520 (2020).
- Y.-C. Chang, S. P. Roberts, B. Stern, I. Datta, and M. Lipson, "Resonance-free light recycling in waveguides," in *CLEO: Science* and Innovations (Optical Society of America, 2017), paper SF1J-5.
- D. A. Miller, "Perfect optics with imperfect components," Optica 2, 747–750 (2015).
- W. Jiang, R. N. Patel, F. M. Mayor, T. P. McKenna, P. Arrangoiz-Arriola, C. J. Sarabalis, J. D. Witmer, R. Van Laer, and A. H. Safavi-Naeini, "Lithium niobate piezo-optomechanical crystals," Optica 6, 845–853 (2019).
- R. Smith, "Use of the acoustooptic light deflector as an optical isolator," IEEE J. Quantum Electron. 9, 545–546 (1973).
- M.-C. Tien, T. Mizumoto, P. Pintus, H. Kromer, and J. E. Bowers, "Silicon ring isolators with bonded nonreciprocal magneto-optic garnets," Opt. Express 19, 11740–11745 (2011).
- S. Ghosh, S. Keyvavinia, W. Van Roy, T. Mizumoto, G. Roelkens, and R. Baets, "Ce:YIG/silicon-on-insulator waveguide optical isolator realized by adhesive bonding," Opt. Express 20, 1839–1848 (2012).
- 44. J. S. Heeks and J. D. Jackson, "Acousto-optic isolator," US patent 4,606,614 (August 19, 1986).
- T. R. O'meara, "Acousto-optical laser isolator," US patent 4,736,382 (April 5, 1988).
- 46. E. Li, B. J. Eggleton, K. Fang, and S. Fan, "Photonic Aharonov–Bohm effect in photon–phonon interactions," Nat. Commun. **5**, 3225 (2014).
- V. Peano, C. Brendel, M. Schmidt, and F. Marquardt, "Topological phases of sound and light," Phys. Rev. X 5, 031011 (2015).
- D. B. Sohn, S. Kim, and G. Bahl, "Time-reversal symmetry breaking with acoustic pumping of nanophotonic circuits," Nat. Photonics 12, 91–97 (2018).
- C. J. Sarabalis, R. Van Laer, and A. H. Safavi-Naeini, "Optomechanical antennas for on-chip beam-steering," Opt. Express 26, 22075–22099 (2018).
- 50. D. B. Sohn and G. Bahl, "Direction reconfigurable nonreciprocal acousto-optic modulator on chip," APL Photon. **4**, 126103 (2019).
- I. A. Williamson, M. Minkov, A. Dutt, J. Wang, A. Y. Song, and S. Fan, "Breaking reciprocity in integrated photonic devices through dynamic modulation," arXiv:2002.04754 (2020).
- W. Fu, Z. Shen, Y. Xu, C.-L. Zou, R. Cheng, X. Han, and H. X. Tang, "Phononic integrated circuitry and spin-orbit interaction of phonons," Nat. Commun. 10, 2743 (2019).